Comparison between SOFI and STORM

Stefan Geissbuehler,^{1,*} **Claudio Dellagiacoma,**^{1} **and Theo Lasser**^{1}

Laboratoire d'Optique Biomédicale, Ecole Polytechnique Fédérale de Lausanne,
Station 17, CH-1015 Lausanne, Switzerland
**stefan.geissbuehler@epfl.ch*

Abstract: A straightforward method to achieve super-resolution consists of taking an image sequence of stochastically blinking emitters using a standard wide-field fluorescence microscope. Densely packed single molecules can be distinguished sequentially in time using high-precision localization algorithms (e.g., PALM and STORM) or by analyzing the statistics of the temporal fluctuations (SOFI). In a face-to-face comparison of the two post-processing algorithms, we show that localization-based super-resolution can deliver higher resolution enhancements but imposes significant constraints on the blinking behavior of the probes, which limits its applicability for live-cell imaging. SOFI, on the other hand, works more consistently over different photo-switching kinetics and also delivers information about the specific blinking statistics. Its suitability for low SNR acquisition reveals SOFI's potential as a high-speed super-resolution imaging technique.

OCIS codes: (180.2520) Fluorescence microscopy; (100.6640) Super-resolution.

References and links

1. S. Hell, "Microscopy and its focal switch," Nat. Methods **6**(1), 24–32 (2009).
2. B. Huang, M. Bates, and X. Zhuang, "Super-resolution fluorescence microscopy," Annu. Rev. Biochem. **78**(1), 993–1016 (2009).
3. G. Patterson, M. Davidson, S. Manley, and J. Lippincott-Schwartz, "Superresolution imaging using single-molecule localization," Annu. Rev. Phys. Chem. **61**(1), 345–367 (2010).
4. L. Schermelleh, R. Heintzmann, and H. Leonhardt, "A guide to super-resolution fluorescence microscopy," J. Cell Biol. **190**(2), 165–175 (2010).
5. M. Gustafsson, "Nonlinear structured-illumination microscopy: wide-field fluorescence imaging with theoretically unlimited resolution," Proc. Natl. Acad. Sci. U.S.A. **102**(37), 13081–13086 (2005).
6. S. W. Hell and J. Wichmann, "Breaking the diffraction resolution limit by stimulated emission: stimulated-emission-depletion fluorescence microscopy," Opt. Lett. **19**(11), 780–782 (1994).
7. E. Betzig, G. Patterson, R. Sougrat, O. Lindwasser, S. Olenych, J. Bonifacino, M. Davidson, J. Lippincott-Schwartz, and H. Hess, "Imaging intracellular fluorescent proteins at nanometer resolution," Science **313**(5793), 1642–1645 (2006).
8. M. Rust, M. Bates, and X. Zhuang, "Sub-diffraction-limit imaging by stochastic optical reconstruction microscopy (STORM)," Nat. Methods **3**, 793–796 (2006).
9. S. Hess, T. Girirajan, and M. Mason, "Ultra-high resolution imaging by fluorescence photoactivation localization microscopy," Biophys. J. **91**(11), 4258–4272 (2006).
10. M. Heilemann, S. V. D. Linde, M. Schüttpelz, R. Kasper, B. Seefeldt, A. Mukherjee, P. Tinnefeld, and M. Sauer, "Subdiffraction-resolution fluorescence imaging with conventional fluorescent probes," Angew. Chem. Int. Ed. Engl. **47**(33), 6172–6176 (2008).
11. R. Wombacher, M. Heidbreder, S. van de Linde, M. P. Sheetz, M. Heilemann, V. W. Cornish, and M. Sauer, "Live-cell super-resolution imaging with trimethoprim conjugates," Nat. Methods **7**(9), 717–719 (2010).
12. F. Aguet, S. Geissbühler, I. Märki, T. Lasser, and M. Unser, "Super-resolution orientation estimation and localization of fluorescent dipoles using 3-D steerable filters," Opt. Express **17**(8), 6829–6848 (2009).
13. B. Huang, W. Wang, M. Bates, and X. Zhuang, "Three-dimensional super-resolution imaging by stochastic optical reconstruction microscopy," Science **319**(5864), 810–813 (2008).

#138247 - $15.00 USD Received 15 Nov 2010; revised 16 Dec 2010; accepted 14 Jan 2011; published 28 Jan 2011

14. S. Pavani, M. Thompson, J. Biteen, S. Lord, N. Liu, R. Twieg, R. Piestun, and W. Moerner, “Three-dimensional, single-molecule fluorescence imaging beyond the diffraction limit by using a double-helix point spread function,” Proc. Natl. Acad. Sci. U.S.A. **106**(9), 2995–2999 (2009).
15. C. Winterflood, T. Ruckstuhl, D. Verdes, and S. Seeger, “Nanometer axial resolution by three-dimensional supercritical angle fluorescence microscopy,” Phys. Rev. Lett. **105**(10), 108103 (2010).
16. G. Shtengel, J. A. Galbraith, C. G. Galbraith, J. Lippincott-Schwartz, J. M. Gillette, S. Manley, R. Sougrat, C. M. Waterman, P. Kanchanawong, M. W. Davidson, R. D. Fetter, and H. F. Hess, “Interferometric fluorescent super-resolution microscopy resolves 3D cellular ultrastructure,” Proc. Natl. Acad. Sci. U.S.A. **106**(9), 3125–3130 (2009).
17. I. Märki, N. L. Bocchio, S. Geissbuehler, F. Aguet, A. Bilenca, and T. Lasser, “Three-dimensional nano-localization of single fluorescent emitters,” Opt. Express **18**(19), 20263–20272 (2010).
18. T. Dertinger, R. Colyera, G. Iyer, S. Weiss, and J. Enderlein, “Fast, background-free, 3D super-resolution optical fluctuation imaging (SOFI),” Proc. Natl. Acad. Sci. U.S.A. **106**(52), 22287–22292 (2009).
19. T. Dertinger, R. Colyer, R. Vogel, J. Enderlein, and S. Weiss, “Achieving increased resolution and more pixels with Superresolution Optical Fluctuation Imaging (SOFI),” Opt. Express **18**(18), 18875–18885 (2010).
20. T. Watanabe, S. Fukui, T. Jin, F. Fujii, and T. Yanagida, “Real-time nanoscopy by using blinking enhanced quantum dots,” Biophys. J. **99**(7), L50–L52 (2010).
21. J. M. Mendel, “Tutorial on higher-order statistics (spectra) in signal processing and system theory: theoretical results and some applications,” Proc. IEEE **79**(3), 278–305 (1991).
22. M. Cheezum, W. Walker, and W. Guilford, “Quantitative comparison of algorithms for tracking single fluorescent particles,” Biophys. J. **81**(4), 2378–2388 (2001).
23. H. M. O’Hare, K. Johnsson, and A. Gautier, “Chemical probes shed light on protein function,” Curr. Opin. Struct. Biol. **17**(4), 488–494 (2007).
24. C. Dellagiacoma, G. Lukinavičius, N. Bocchio, S. Banala, S. Geissbühler, I. Märki, K. Johnsson, and T. Lasser, “Targeted photoswitchable probe for nanoscopy of biological structures,” ChemBioChem **11**(10), 1361–1363 (2010).
25. S. V. D. Linde, S. Wolter, M. Heilemann, and M. Sauer, “The effect of photoswitching kinetics and labeling densities on super-resolution fluorescence imaging,” J. Biotechnol. **149**(4), 260–266 (2010).
26. R. Thompson, D. Larson, and W. Webb, “Precise nanometer localization analysis for individual fluorescent probes,” Biophys. J. **82**(5), 2775–2783 (2002).
27. C. E. Shannon, “Communication in the presence of noise,” Proc. IEEE **86**(2), 447–457 (1998).
28. M. Heilemann, S. V. D. Linde, A. Mukherjee, and M. Sauer, “Super-resolution imaging with small organic fluorophores,” Angew. Chem. Int. Ed. Engl. **48**(37), 6903–6908 (2009).

---

1. Introduction

Advances in far-field fluorescence microscopy have produced a number of techniques capable of imaging features with a resolution well beyond the diffraction limit [1–4]. Switching the fluorescence of single emitters sequentially on and off in either a targeted [5, 6] or stochastic manner [7, 8] enables the distinction of objects within a diffraction-limited spot.

In photo-activation localization microscopy (PALM and FPALM) [7, 9] or stochastic optical reconstruction microscopy (STORM and dSTORM) [8, 10], only a sparse, stochastic subset of fluorophores is active in a certain time interval. The diffraction patterns of individual molecules appear isolated, and their positions can be computed with high localization accuracy. Taking multiple acquisitions and combining all the localizations into a composite image results in a high- resolution image of the specimen.

Improvements of the blinking probes and chemical buffers recently enabled live-cell STORM [11]. Further developments enabling 3D imaging include advanced localization algorithms [12], PSF engineering [13, 14], super-critical angle microscopy [15] and interferometric imaging techniques [16, 17].

Dertinger et al. introduced an alternative concept for resolution enhancement based on the statistical analysis of temporal fluorescence fluctuations [18, 19]. Super-resolution optical fluctuation imaging (SOFI) demonstrated theoretically unrestricted resolution by computing temporal cumulants, or spatio-temporal cross-cumulants. Because a single molecule spatio-temporally correlates only with itself, a high-resolution image can be generated directly from the temporal correlations of each pixel trace. By computing the n-th order cumulants, only point-spread functions raised to the power of n are retained, which leads to a $\sqrt{n}$-fold resolution improvement. This effect is a direct consequence of the additivity of cumulants when dealing with independently blinking emitters. Computing higher-order moments, or correlations, would give rise to mixed terms stemming from multiple emitters. Unlike localization-based techniques, SOFI enables the separation of fluorophores with spatially overlapping diffraction patterns and only requires dark-state lifetimes on the order of the frame rate. Furthermore, it has the potential to be faster than localization microscopy. A recent variant of SOFI called variance imaging for super-resolution (VISION) demonstrated a remarkable 80ms temporal resolution [20]. It is based on a multiple variance calculation. However, like higher-order moments, multiple variances are not additive, and thus, the effective spatial resolution enhancement is limited.

In this article, we compare the two post-processing techniques used for STORM and SOFI evaluated on the same measurements. By applying the techniques on data sets obtained from simulations and experiments, we present a direct comparative study of both procedures, identifying the advantages and limitations for each case.

2. Materials and methods

2.1. Algorithms

2.1.1. SOFI algorithm

Initially, SOFI consisted of computing higher-order autocumulants [18], where the achievable resolution was limited by the effective pixel size of the detector. Recently, it has been shown that this limitation can be circumvented using spatio-temporal cross-cumulants (XC-SOFI) for generating a finer sampling grid. Furthermore, a simple reweighting scheme in the Fourier domain of the n-th order SOFI image has been introduced, which modifies the resulting SOFI PSF to yield the original microscope PSF with an n-fold reduced size, corresponding to a resolution improvement by a factor of n [19]. Here we implemented those recent developments, calculated spatio-temporal cross-cumulants to generate inter-pixels and estimated the point-spread function, which is necessary for the subsequent Fourier reweighting (FRW).

A scheme illustrating the different steps of the SOFI algorithm is depicted in Fig. 1. The computation of different combinations of spatio-temporal cross-cumulants of each pixel with $n-1$ of its neighboring pixels enables the construction of an n-fold finer sampling grid in the final image (see Fig. 2). Due to the spatial decrease of correlation, the inter-pixels generated by cross-cumulants are lower in amplitude than the pixels generated by the auto-cumulants and thus need to be corrected by a distance factor (Fig. 1, step 3). Using a model (e.g., Gaussian) of the microscope's point-spread function and varying its parameters, these correction factors can be iteratively optimized until all pixels have similar weights. We have used the 2D Laplacian as a cost-function of the optimization algorithm, which turned out to be robust. The resulting estimation of the point-spread function is used in the Fourier reweighting (Fig. 1, step 4).

2.1.2. Localization algorithm

STORM processing, similar to single-molecule tracking algorithms, consists of a frame-by-frame image segmentation and subsequent single-molecule localization using Gaussian fitting [22]. Figure 3 illustrates the main steps of our implementation. Image segmentation involves filtering with a Laplacian of Gaussian to simultaneously reduce noise and enhance isolated single emitter signals. After threshold background subtraction, the remaining image segments of reasonable sizes are analyzed. The center of gravity of a segment yields a first estimate of the fluorophore's position, which is introduced as an initial value in the Gaussian fit (Fig. 3, step 2). We applied an unweighted least-squares optimization to estimate the amplitude, position, waist

#138247 - $15.00 USD Received 15 Nov 2010; revised 16 Dec 2010; accepted 14 Jan 2011; published 28 Jan 2011

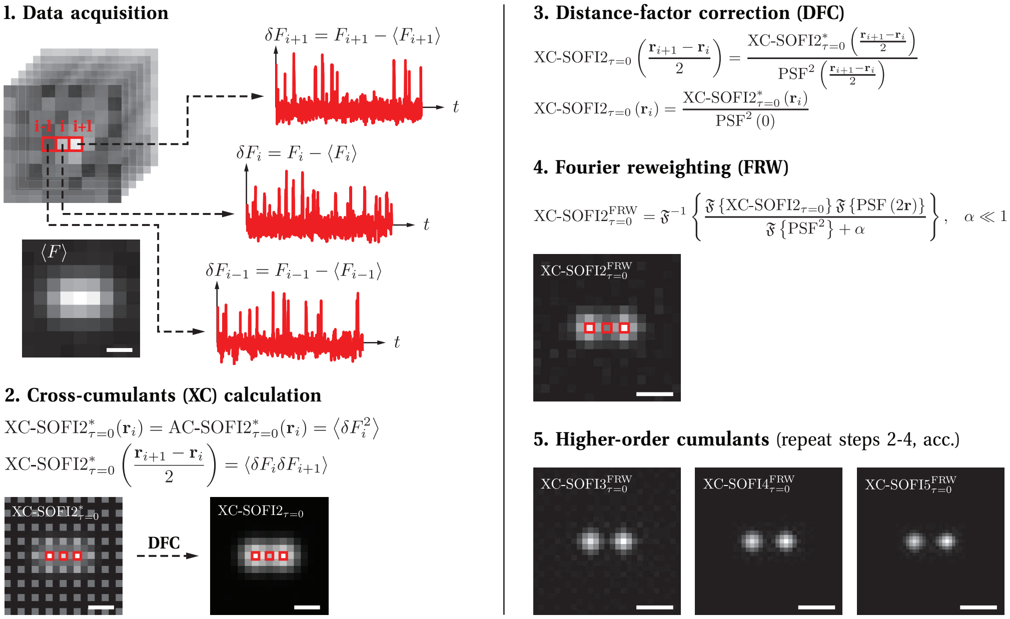

Fig. 1. The different steps of calculating cross-cumulant SOFI with Fourier reweighting (XC-SOFI-FRW), illustrated for the second order. Before the computation of cross-cumulants, the mean is subtracted from the data. Using different combinations of cross-cumulants between pixels gives rise to an inhomogeneous weight distribution (step 2), which needs to be corrected by a distance factor (step 3). The distance-factor correction also provides an estimation of the system's PSF. Fourier reweighting (FRW) enables the modification of the SOFI equivalent PSF to retrieve the microscope's PSF with an *n*-fold reduced size (step 4). Higher-order cumulants are computed using the exact formulation described in [21]. *Scale bars: 200 nm.*

and background using the Levenberg-Marquardt algorithm. Estimates of width and amplitude that varied by more than a factor of two from their expected values were discarded to reduce the number of false positives. The estimated single-molecule positions were mapped into a high-resolution image (Fig. 3, step 3).

2.2. *Simulation*

Based on a simulation, we investigated the performance of the SOFI and STORM algorithms under the aspects of photo-switching kinetics, labeling density and signal-to-noise ratio. The simulation generates image sequences of randomly blinking fluorophores that are placed arbitrarily on two parallel bands, each 0.04 Airy units wide, at different separation distances. The fluorophore blinking behavior was simulated as a time-continuous Markov process between on and off states using a 100-fold temporal oversampling. The average blinking rate is then given by

$$k = \frac{k_{on} k_{off}}{k_{on} + k_{off}}, \tag{1}$$

where $k_{on} = \tau_{off}^{-1}$ denotes the rate at which the fluorophore is transferred from the off state back to the on state and vice versa for $k_{off} = \tau_{on}^{-1}$. k was fixed to half the sampling rate (f) but was not synchronized with the acquisition time intervals. The number of emitted photons per fluorophore followed a Poisson probability-density distribution with an average photon count rate

#138247 - $15.00 USD Received 15 Nov 2010; revised 16 Dec 2010; accepted 14 Jan 2011; published 28 Jan 2011

(a) Cross-cumulant combinations with repetitions

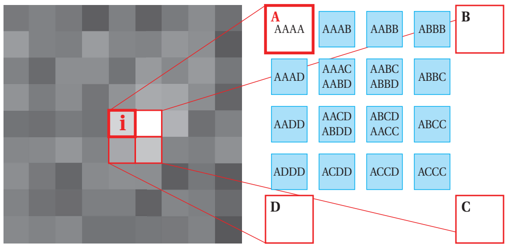

(b) Cross-cumulant combinations without repetitions

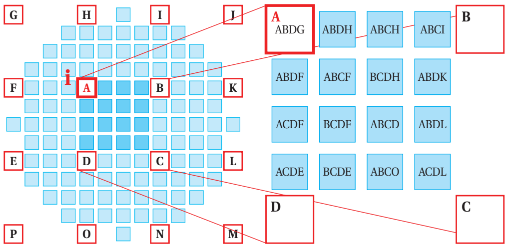

Fig. 2. Fourth-order cross-cumulant combinations for pixel *i* with or without repetitions. Different combinations within a neighborhood matrix of *i* can be used to generate 15 inter-pixels in between the original pixel matrix (ABCD). Combinations leading to the same inter-pixel are averaged. (a) All *n*-combinations within a 2x2 neighborhood (ABCD) starting with A and allowing for repetitions are computed. This scheme can be expanded easily to any order *n*. Due to the presence of autocumulants, this method does not suppress shot noise very well unless non-zero time lags are used. (b) The different combinations within a 4x4 neighborhood of pixel i can be used to generate inter-pixels in a circular arrangement (left). By excluding repetitions (autocumulants), shot noise is suppressed much better. For computational reasons, only combinations featuring the shortest sum of distances with respect to their corresponding inter-pixels are considered. By considering more combinations and averaging over the corresponding cross-cumulants, even more noise could be eliminated. Further simplification can be done by considering only combinations leading to the 15 inter-pixels within ABCD (right). This scheme is expandable until order 10. To go beyond this range, the size of the neighborhood has to be increased.

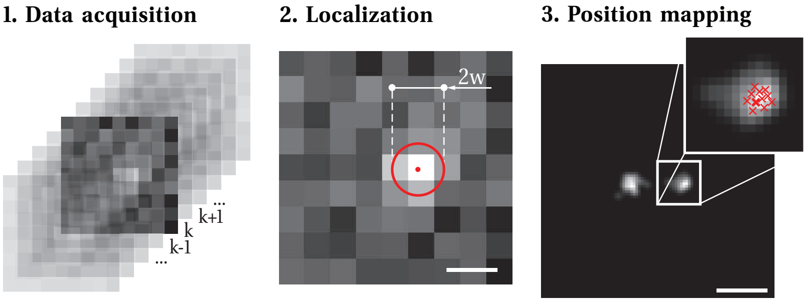

Fig. 3. STORM-principle: The image sequence is processed frame by frame. For the localization, the images are segmented and each isolated diffraction pattern is fitted to a parameterized Gaussian PSF model (step 2). The determined single-molecule positions are combined in a composite image with a ten-fold finer sampling grid (step 3). *Scale bars: 200 nm.*

of 9 kHz in the on state. Similar to measurements, a constant background of 40% of the average molecular amplitude and shot noise was added. For simplicity, we used a Gaussian PSF model with a full-width at half-maximum (FWHM) equal to one Airy unit (237 nm; corresponding to a numerical aperture (NA) of 1.49 and an emission wavelength of 580 nm). The pixel size was 100 nm. For computational ease and to limit the length of the image sequences, we applied generally low labeling densities (5-20/μm), which allow longer fluorophore on-times with respect to their off-times, i.e., a low rate ratio

$$r = \frac{k_{off}}{k_{on}} = \frac{\tau_{off}}{\tau_{on}}. \qquad (2)$$

However, we expect the effect to be similar at higher labeling densities if accordingly higher rate ratios and sequence lengths are used.

We compared the *relative visibility* v (in the following referred to as visibility) of the projected line profiles, defined as

$$v_0 = 0.5\frac{I_{max,1} - I_{min}}{I_{max,1} + I_{min}} + 0.5\frac{I_{max,2} - I_{min}}{I_{max,2} + I_{min}} \qquad (3)$$

$$v = v_0 \left(\frac{\min\{\frac{I_{max,1}}{I_1}, \frac{I_{max,2}}{I_2}\}}{\max\{\frac{I_{max,1}}{I_1}, \frac{I_{max,2}}{I_2}\}} \right)^{\mathrm{sign}\{v_0\}}, \qquad (4)$$

where $I_{max,1}, I_{max,2}, I_{min}, I_1$ and I_2 are defined according to Fig. 4.

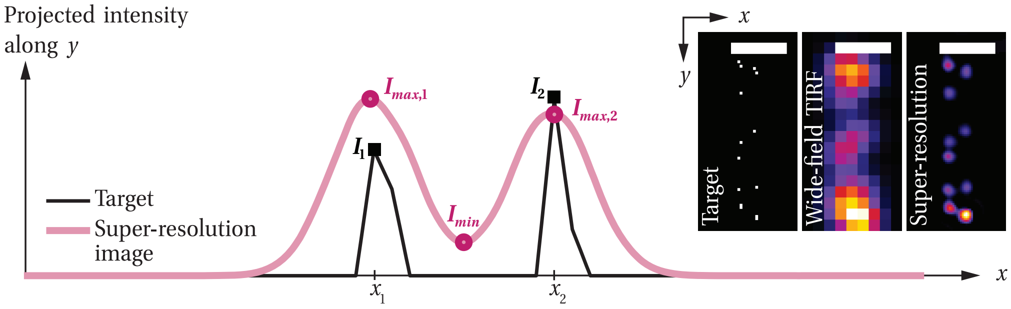

Fig. 4. The visibility defined in Eq. (4) serves as a benchmark for comparing the different algorithms. The line profiles are obtained by projecting the images along the y direction. $I_{max,1}$ and $I_{max,2}$ are obtained by taking the mean intensity at the known positions of the lines (x_1 and x_2) and I_{min} is the mean intensity between $0.4(x_1 + x_2)$ and $0.6(x_1 + x_2)$. *Scale bars: 500 nm.*

2.3. Experiments

We used a custom-designed total-internal-reflection fluorescence (TIRF) microscope in epi-illumination with an oil-immersion objective (Olympus 60x1.49) and two laser excitation sources. Fixed human osteosarcoma cells (U2OS) expressing a β-tubulin-SNAP tag [23] have been labeled with a photo-switchable probe (BG-Cy3-Cy5) and an imaging buffer containing mercaptoethanol, and an oxygen-scavenging system was used to increase the dark state lifetime of Cy5. All experimental details can be found in [24].

3. Simulation results

3.1. Effect of photo-switching kinetics

In Figs. 5 and 6, we compare the effects of varying the rate ratio on the visibility of the two lines in STORM and the different SOFI orders. Van de Linde et al. [25] have already shown that a high rate ratio is crucial for successful STORM imaging, as is confirmed by Figs. 5a, 6d, and 6f. Due to the stochastic nature of the photo-switching fluorophores, it is always possible to have multiple emitters in a diffraction-limited spot. If they are too close to be identified as an agglomeration, the Gaussian fit results in a false localization. The number of false localizations increases with lower rate ratios. At a specific cut-off rate ratio, where multiple emitters are always present in a diffraction-limited spot, STORM fails completely (Fig. 5a at $r < 1$ and Fig. 6d).

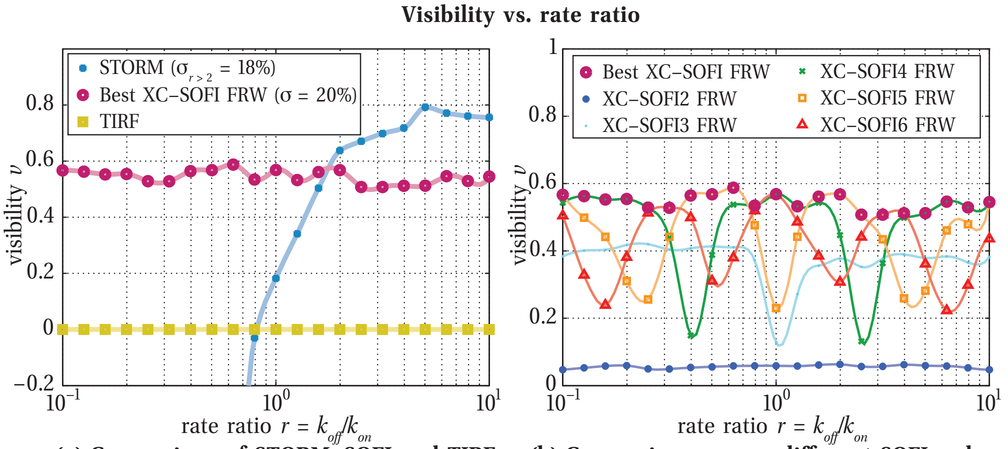

(a) Comparison of STORM, SOFI and TIRF **(b) Comparison among different SOFI orders**

Fig. 5. Comparison of the visibility versus rate ratio. The best XC-SOFI is obtained by the SOFI order yielding the highest average relative visibility for a specific set of simulation parameters. σ denotes the average relative standard deviation. *Fixed simulation parameters:* $k/f = 0.5$, *line separation: 0.6 Airy units, labeling density:* $5/\mu\text{m}$, *1000 frames, 50 realizations per point.*

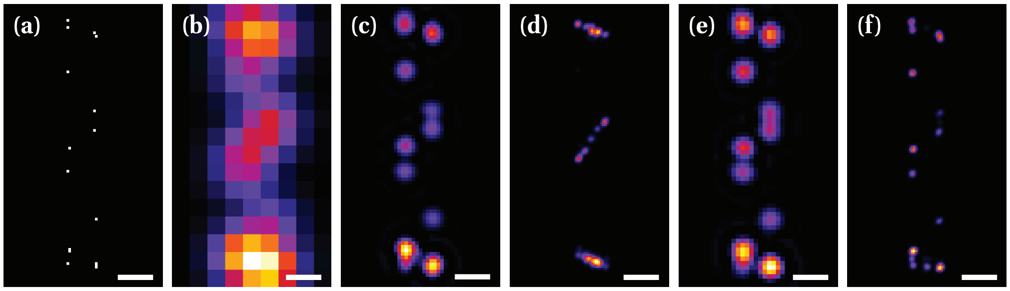

Fig. 6. Visual comparison of SOFI and STORM reconstructions at different rate-ratios. (a) Target structure. (b) Summed TIRF. (c) XC-SOFI5 FRW, $r = 0.6$. (d) STORM, $r = 0.6$. (e) XC-SOFI4 FRW, $r = 10$. (f) STORM, $r = 10$. *Scale bars: 200 nm.*

SOFI, on the other hand, is more robust. Considering different SOFI orders, the visibility is almost independent of the rate ratio (see Fig. 5a), which therefore relaxes the photo-physical

#138247 - $15.00 USD Received 15 Nov 2010; revised 16 Dec 2010; accepted 14 Jan 2011; published 28 Jan 2011

constraints of the emitter. Figure 5b illustrates how different SOFI orders can be used to characterize the blinking nature and statistics. For example, if the blinking is symmetric ($k_{on} = k_{off}$), the skewness or third-order is zero, leading to a visibility $v = 0$. This result is similar to other odd higher-order cumulants, where an asymmetry must be present. For the second-order, the rate ratio does not have any effect on the visibility as long as it is the same for all molecules because the variance of the blinking is the measured quantity.

3.2. *Effect of labeling density*

The effect of the labeling density is depicted in Figs. 7 and 8. In STORM imaging, the labeling density is directly linked to the cut-off rate ratio [25]. Higher labeling densities require higher rate ratios to ensure the occurrence of isolated single-emitter diffraction patterns. In the example in Fig. 7a, with a rate ratio of 2, the labeling density should not exceed $10/\mu$m, otherwise false localizations predominate (Fig. 8h).

In SOFI, the decrease in visibility with increasing labeling density is less pronounced and is due to the decreased relative intensity fluctuations. Figure 7b reveals a stronger decrease for higher orders.

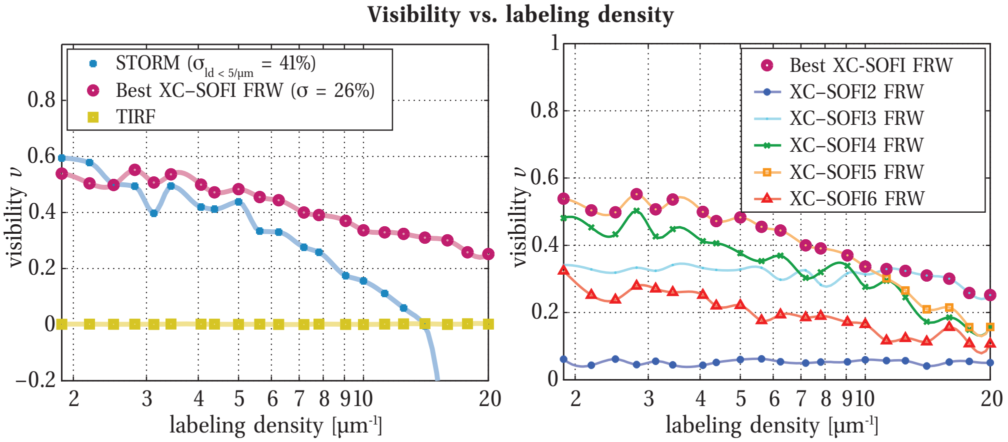

(a) Comparison of STORM, SOFI and TIRF **(b) Comparison among different SOFI orders**

Fig. 7. Comparison of the visibility versus labeling density. The best XC-SOFI is obtained by the SOFI order yielding the highest average relative visibility for a specific set of simulation parameters. σ denotes the average relative standard deviation. *Fixed simulation parameters:* $k/f = 0.5$, $r = 2$, *line separation: 0.6 Airy units, 1000 frames, 25 realizations per point.*

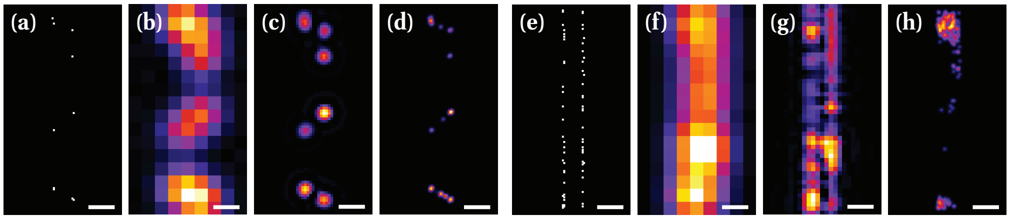

Fig. 8. Visual comparison of SOFI and STORM reconstructions at different labeling densities. Labeling density: (a-d) $3/\mu$m, (e-h) $20/\mu$m. (a,e) Target structure. (b,f) Summed TIRF. (c) XC-SOFI5 FRW. (g) XC-SOFI3 FRW. (d,h) STORM. *Scale bars: 200 nm.*

3.3. *Effect of the signal-to-noise ratio*

In single-molecule localization, the accuracy essentially scales inversely with the number of collected photons [26]. A sufficiently high signal-to-noise ratio per frame has to be guaranteed to estimate the position with high precision. Similar to fluorescence correlation spectroscopy (FCS) analyzing fast fluorescence intensity fluctuations, SOFI can be expected to work with a much lower SNR than localization microscopy. Figure 9 illustrates the effect of the peak signal-to-noise ratio (pSNR) on the visibility for STORM and the different SOFI orders. Figure 9b shows that SOFI orders 2 to 4 can be used to generate super-resolution images until 10 to 20 dB below the minimum pSNR needed for STORM. This implies that when using a fast camera, SOFI could have a significant speed advantage over localization microscopy. For example, a drop of 50% in visibility for SOFI order 3 occurs only at about 5 dB, whereas for STORM this already occurs at 22 dB. Assuming a constant detector sensitivity and a shot-noise-limited system with a square-root dependence of SNR on time, the acquisition rate could then be about 45 times higher. In this simulation, we used the cross-cumulant approach without repetitions to efficiently eliminate shot noise. The low visibilities for SOFI orders 5 and 6 are due to cross-cumulant combinations between pixels further apart than the FWHM of the PSF (here, 2.3 px). This issue might be addressed using non-zero time lags and using the combination scheme with repetitions.

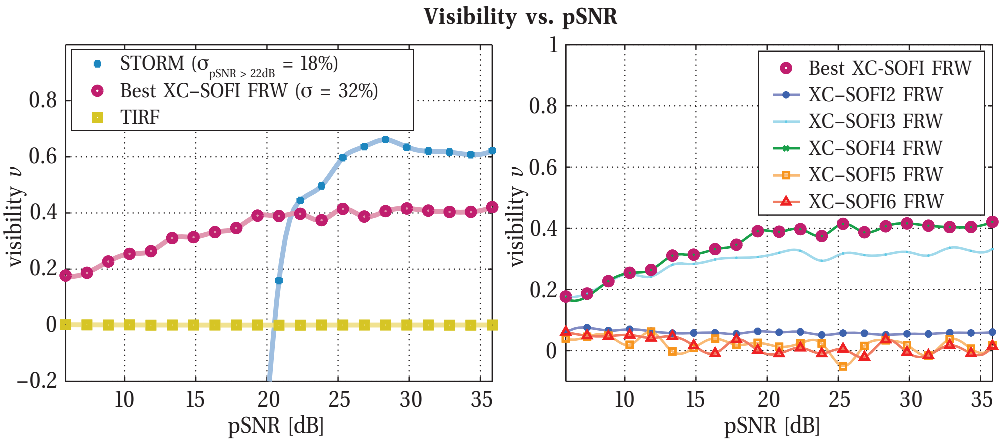

(a) Comparison of STORM, SOFI and TIRF **(b) Comparison among different SOFI orders**

Fig. 9. Comparison of the visibility versus pSNR. XC-SOFI has been computed using cross-cumulant combinations without repetitions. The best XC-SOFI is obtained by the SOFI order yielding the highest average relative visibility for a specific set of simulation parameters. σ denotes the average relative standard deviation. *Fixed simulation parameters:* $k/f = 0.5$, $r = 6.7$, *line separation: 0.6 Airy units, labeling density:* $5/\mu\text{m}$, *2000 frames, 50 realizations per point.*

3.4. *Effect of the line separation distance*

In localization-based super-resolution microscopy, the resolution is often estimated from the accuracy of single-molecule localization. This estimation assumes that the dark time is sufficiently high such that single emitters still appear isolated in time in the regions of highest labeling densities. The localization accuracy cannot be linked to the minimum distance between two objects that are still distinguishable as long as the labeling densities and photo-switching kinetics are unknown. Using our simulation to compare the visibility versus the line separation distance enables the analysis of the effective resolutions of STORM and SOFI for given on- and off-rates, frame rate, labeling density, sequence length and SNR. Figure 10 shows an example in which the rate ratio is sufficiently high for STORM to resolve the structures of a given labeling density until the separation distance gets close to the FWHM localization accuracy limit. Table 1 lists the corresponding limits of resolution in Airy units. The values correspond to the separation distances, where the visibility grows larger than 10^{-3}. In the case of SOFI, small oscillations around zero visibility can be seen when approaching the resolution limit (see Fig. 10b). These oscillations are due to numerical effects arising from sampling close to the Nyquist limit, which corresponds to twice the resolving power. Increasing the magnification of the microscope would reduce these oscillations. The resolution limits of the different Fourier-reweighted SOFI orders were estimated by the points of deflection of the Fourier reweighted (XC-SOFI FRW) from the untreated SOFI (XC-SOFI) visibility curves.

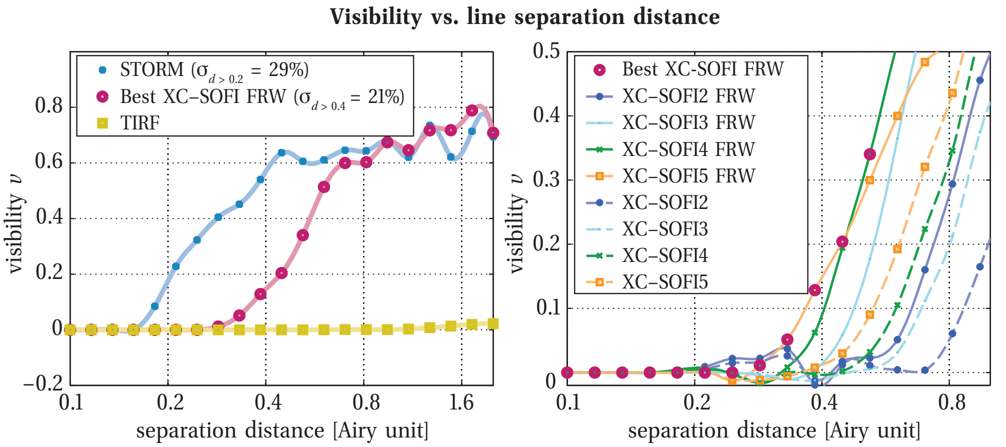

(a) Comparison of STORM, SOFI and TIRF **(b) Comparison among different SOFI orders**

Fig. 10. Comparison of the visibility versus line separation distance. The best XC-SOFI is obtained by the SOFI order yielding the highest average relative visibility for a specific set of simulation parameters. σ denotes the average relative standard deviation. *Fixed simulation parameters:* $k/f = 0.5$, $r = 6.7$, *labeling density:* $5/\mu\text{m}$, *2000 frames, 50 realizations per point.*

Table 1. Limits of resolution in Airy units and the corresponding improvement factors with regards to wide-field TIRF

	TIRF	XC-SOFI-FRW				STORM
		2	3	4	5	
resolution limit	1.00	0.47	0.33	0.28	0.24	0.16
improvement	-	2.1x	3.0x	3.6x	4.2x	6.4x

4. Experimental results

The experiments with microtubule structures in human osteosarcoma cells (U2OS) showed significant resolution and contrast enhancements for both STORM and SOFI in comparison to the wide-field image (Fig. 11). Regions of low microtubule density led to well resolved STORM images (e3), whereas the imaging of crossing structures, or regions of high labeling densities, was more problematic due to rarely isolated single emitter patterns (e2). Apparently, the rate ratio was not sufficiently high in these regions. The third order SOFI image reveals the presence of two closely spaced microtubuli at the pointing arrow in (c2). SOFI worked consistently all over the image up to order 3. At higher orders, dimmer and/or weakly fluctuating molecules get lost in the background, and the imaged structures lose connection (see Fig. 11b–11d). This is mainly due to the fact that SOFI order *n* raises the heterogeneities in molecular brightness to the power of *n*, which makes it increasingly difficult to display continuous structures for higher orders without compromising the apparent resolution.

The last row in Fig. 11 shows the transversal intensity distributions and FWHMs of a single microtubule, averaged over 400 nm along the structure.

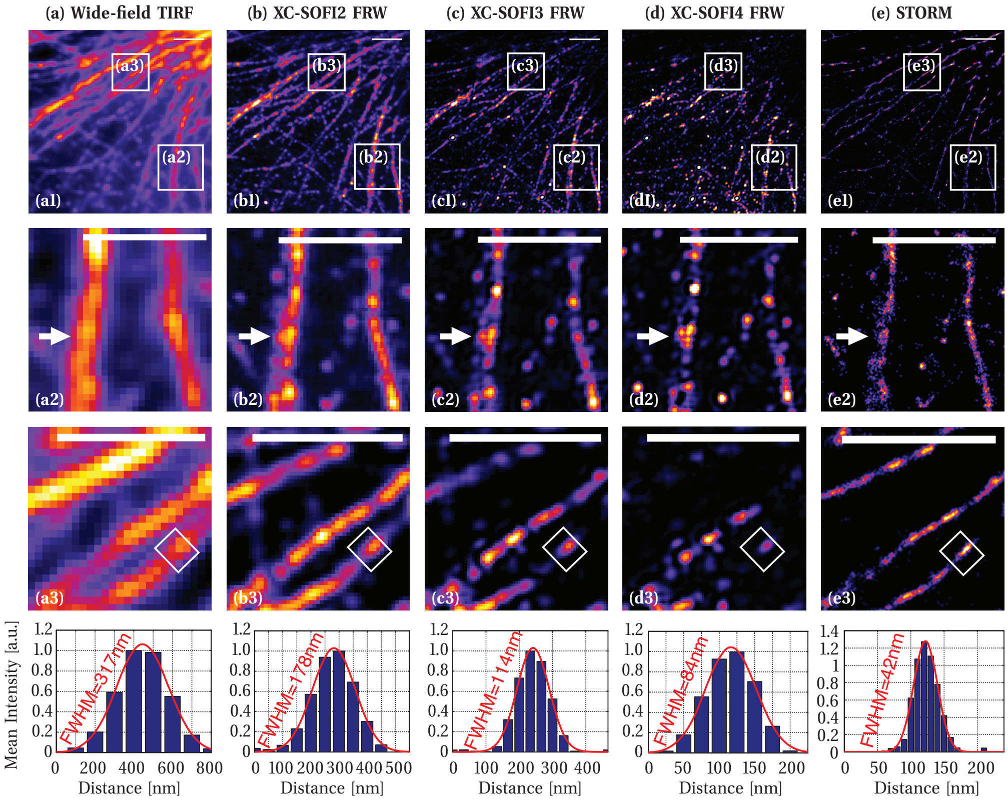
(a) Wide-field TIRF **(b) XC-SOFI2 FRW** **(c) XC-SOFI3 FRW** **(d) XC-SOFI4 FRW** **(e) STORM**

Fig. 11. Microtubule structures in human osteosarcoma cells: Experimental demonstration of resolution improvements for SOFI and STORM. Row 2 illustrates the effect of insufficient rate ratios at high labeling densities, which makes it impossible for STORM to resolve the two closely spaced microtubuli at the pointing arrow. Regions of well-separated structures are less problematic (row 3). Row 4 shows the transversal intensity distribution of a microtubule (white box in row 3) fitted to a Gaussian. The intensity distribution is averaged over a length of 400 nm along the structure. *Scale bars: 2* μm

5. Discussion

According to the Nyquist-Shannon sampling theorem [27], the average distance between neighboring fluorophores attached to a structure of interest must not exceed half of the desired resolution. In order to ensure effective resolutions well below the diffraction limit, very high labeling densities are needed. For STORM, diffraction patterns of individual fluorophores have to appear isolated, which implies the necessity of very stable and long-lived dark states, respectively high rate ratios. This can be achieved using high irradiation intensities and special chemical buffers with thiol compounds and oxygen removal. As a consequence, the applicability on living organisms is limited [28]. In the case of SOFI, the requirements concerning blinking and labeling density are more relaxed. The only prerequisite is to have stochastically and independently fluctuating light emitters with a temporally resolvable blinking, which may be achieved without or with less toxic imaging buffers and a variety of probes. Unlike localization microscopy, where one has to wait until each emitter appeared isolated at least once in the image sequence, the information of multiple overlapping emitters can be captured simultaneously and hence suggests a reduced total acquisition time. Furthermore, localization requires a relatively high pSNR of at least 20dB. As we have seen from the simulations, this limit is much lower for SOFI, which allows a significantly increased acquisition rate.

Concerning the possible effective resolution improvements, STORM usually outperforms SOFI provided that the requirements are met for a specific sample. Although by computing higher-order SOFI images a similar resolution enhancement should theoretically be possible, there are a number of factors limiting the maximum order. The presence of heterogeneities in blinking statistics and fluorescence intensities usually leads to discontinuities in the image structures when going beyond the 4th order, as we have seen in the experiments. While the information content is conserved even in higher-orders, visualizing nonlinear intensity distributions without compromising the apparent resolution is difficult. Additional limitations of the maximum order are the computational effort and the number of frames required, which both increase significantly with the SOFI order. Also, when using cross-cumulant combinations without repetitions, one should ensure that only a neighborhood within the microscope's PSF is considered, as seen in Fig. 9b. Furthermore, if the noise contributions become stronger, Fourier reweighting starts to fail at higher orders [19]. To address these issues and to increase the final resolution of SOFI, one may try integrating over several time delays and/or averaging over multiple cross-cumulant combinations to further reduce noise and equalize blinking heterogeneities. Also the visualization may be improved, e.g. by using colormaps that are specifically adapted to SOFI imaging.

Another important property of SOFI is its strong, inherent optical sectioning which may be suitable for bright-field illumination and 3D imaging over a large depth range. On the contrary, localization microscopy usually needs an additional means of optical sectioning, such as TIR or spinning-disk confocal illumination, in order to avoid an increased overlapping of single emitters and to ensure a correct functioning of the algorithm. However, the localizations may then even be performed in 3D using a more accurate PSF model, and/or a modified optical system generating an engineered PSF that is more sensitive to changes in the axial position. This enables the reconstruction of a 3D slice, out of 2D data, whereas in SOFI one has to scan axially to render 3D data.

6. Conclusion

In this study, we compared two post-processing algorithms for super-resolution microscopy, STORM and SOFI. Both techniques can be readily applied to standard fluorescence microscopes. We showed that localization microscopy with photo-switchable probes requires highly stable dark states and thereby imposes significant constraints on the sample preparation for successful application in living cells. To estimate the effective resolution of STORM, it is necessary to identify the photo-switching kinetics and labeling densities. In our simulation we showed that the different SOFI orders could be used to determine the blinking statistics, which may be useful in evaluating the applicability of STORM on a measured image sequence. If the sample requirements are met, localization microscopy can deliver the highest resolution in state-of-the-art wide-field light microscopy. Nevertheless, SOFI proved its potential as an attractive alternative to localization microscopy because it works consistently over a wide range of blinking statistics and tolerates much lower SNRs, which reveals its potential for high-speed super-resolution microscopy. Furthermore, the inherent optical sectioning property of SOFI enables 3D imaging without modifying the optical setup. Altogether, SOFI is an attractive and straightforward approach to fast three-dimensional super-resolution imaging of biological samples.

Acknowledgement

This research was supported by the Swiss National Science Foundation SNSF (Synergia project CRSII3 125463; K-23K1-116242/1; 315200-116729). We acknowledge Prof. Jörg Enderlein and Dr. Thomas Dertinger for stimulating discussions and Dr. Grazvydas Lukinavicius for providing the biological samples. Furthermore, we thank Dr. Noelia Bocchio, Dr. Marcel Leutenegger, Matthias Geissbuehler and Dr. Iwan Märki for their constructive comments on the manuscript.